Geochimica et Cosmochimica Acta 411 (2025) 86–99

Contents lists available at ScienceDirect

Geochimica et Cosmochimica Acta

journal homepage: www.elsevier.com/locate/gca

Microfluidic experiments to rationalize coupled mineral dissolution and precipitation with gas exsolution

Jenna Poonoosamy [a,*], Ryan Santoso [a], Alexander Kaspor [a], Lara Wegner [a], Romain V.H Dagnelie [b], G.Dan Miron [c]

[a] Institute of Fusion Energy and Nuclear Waste Management (IFN-2): Nuclear Waste Management, Forschungszentrum Jülich GmbH, 52425 Jülich, Germany
[b] Université Paris-Saclay, CEA, 91191 Gif-sur-Yvette, France
[c] Laboratory for Waste Management, Paul Scherrer Institut, CH-5232 Villigen PSI, Switzerland

ARTICLE INFO

Associate editor: Carl Steefel

Keywords:
Lab on a chip
Microfluidics
Carbonate minerals
Gas bubble
Barite

ABSTRACT

Coupled mineral dissolution and precipitation with gas exsolution are relevant subsurface processes occurring during CO_2 sequestration, hydrogen storage, and radioactive waste disposal. While gas exsolution during mineral dissolution has been studied, its interaction with concurrent mineral precipitation remains unclear. Here, we use a microfluidic reactor with real-time optical and 3D Raman imaging to study witherite dissolution in sulfate-rich acidic solutions, leading to barite precipitation and CO_2 exsolution. "Cauliflower-like structures" are observed, in which barite encrusts gas bubbles, forming mineral-coated structures, a phenomenon that can be explained by the electric double layer of gas bubbles that causes local increase in saturation with respect to barite, favoring precipitation. Raman imaging reveals water droplets – cloud-like dispersions – trapped inside the mineral-encrusted bubbles. In addition to the cauliflower-like structures that trap gas bubbles, we identified conditions under which the system transitions to a multiphase flow regime, i.e., gas transport along with the liquid flow. Geochemical modeling shows that such processes are heavily coupled with the exsolution of CO_2 and controlled by the acidity. The cauliflower-like structures only occur when the precipitation rate is faster than dissolution. The precipitation as cauliflower-like structure is caused by competition between the rate of gas production from witherite dissolution and the barite growth rate. These cauliflower-like structures can reduce mineral dissolution, potentially slowing down the corrosion of waste canisters, but also impeding CO_2 storage and hydrogen recovery by clogging pore spaces.

1. Introduction

Coupled mineral dissolution and precipitation, characterized by the dissolution of a primary mineral and the precipitation of a secondary mineral on its surface, is relevant for various natural and anthropogenic subsurface systems (Guren et al., 2020; Hellmann et al., 2012; Konrad-Schmolke et al., 2018; Putnis and Putnis, 2022; Renard et al., 2019; Ruiz-Agudo et al., 2014; Schott et al., 2009; Xing et al., 2021; Zhang et al., 2020). This coupled process can result in the release of gases as by-products. For example, during the serpentinization of ultramafic rocks, hydrogen can be produced naturally (Antwi et al., 2025; Lefeuvre et al., 2022; Osselin et al., 2022) and similar gas production can occur during the anoxic corrosion of metallic waste containers in deep geological repositories for radioactive waste (Guo et al., 2020; Xu et al., 2008). In both scenarios, the Schikorr reaction (Li et al., 2023) occurs where $Fe(OH)_2$ is oxidized into magnetite. Gas exsolution can also occur during CO_2 sequestration in deep saline aquifers (Xu et al., 2017) and within sandstone formations (Gholami and Raza, 2022). Similar coupled processes are observed in geothermal and hydrothermal systems, where gas exsolution (e.g., CO_2 or H_2S) is followed by rapid mineral precipitation of barite in shallow vents (e.g. Panarea, Aeolian Islands), in mineral-rich brines at mid-ocean ridges (Savelli et al., 1999), as well as in shallow-water environments where fluid boiling generates a water vapor phase, such as offshore Iceland, the Mediterranean Sea, and Indonesia (Hannington et al., 2001; Stoffers et al., 2006; Kilias et al., 2013).

Secondary mineral formation has substantial effects on subsurface solute transport and geochemistry (Pina et al., 1998; Putnis et al., 1992). It can either develop porosity and fractures that enable fluid exchange and thereby completely replace the primary mineral, or form armoring layers that shield the primary mineral from further dissolution

---

* Corresponding author.
E-mail address: j.poonoosamy@fz-juelich.de (J. Poonoosamy).

https://doi.org/10.1016/j.gca.2025.10.025
Received 3 July 2025; Accepted 19 October 2025

(Boampong et al., 2024; Deng et al., 2022; Forjanes et al., 2020; Putnis et al., 1992; Steefel and Yang, 2021; Weber et al., 2023). While such processes have been extensively studied, there is still much uncertainty about the fate of gases produced during these reactions. Specifically, it remains unclear whether the produced gas dissolves, accumulates and becomes trapped within the newly formed secondary minerals, or is instead transported through the surrounding fluid. Previous studies have explored the fate of gas production resulting from mineral dissolution, highlighting how multiphase flow dynamics influence gas transport, reaction rates, and mineral stability (Jiménez-Martínez et al., 2020; Soulaine et al., 2018; Xu and Balhoff, 2022). However, the coupling of this phenomenon with simultaneous mineral precipitation has not been explored to our knowledge.

Coupled mineral dissolution and precipitation can significantly impact rock permeability and diffusivity, affecting the effectiveness of subsurface energy storage and extraction (Beckingham, 2017; Lönartz et al., 2023; Poonoosamy et al., 2020a; Poonoosamy et al., 2020b; Poonoosamy et al., 2022; Steinwinder and Beckingham, 2019). For example, trapped gases may impair the functionality of systems used for CO_2 sequestration, hydrogen storage, and even the long-term containment of radioactive waste (Gershenzon et al., 2017). A comprehensive understanding of multi-phase fluid flow, gas generation, and reactive transport under evolving geochemical conditions is therefore essential for optimizing these applications.

Developing predictive models that accurately capture mineral dissolution, precipitation, and gas exsolution remains a challenge due to the complexity and non-linearity of these interactions (Seigneur et al., 2019; Steefel, 2019). While investigations of natural and technical materials, such as rocks in geological formations and concrete, offer valuable insights, they often provide only a phenomenological understanding. To explore the underlying mechanisms in greater detail for theoretical model development, researchers often turn to simplified "model systems", which isolate specific processes under controlled chemical and hydraulic conditions (Katz et al., 2011; Muniruzzaman et al., 2014; Poonoosamy et al., 2016; Poonoosamy et al., 2015; Tartakovsky et al., 2008). These model systems provide an ideal platform for investigating complex processes and offer valuable insights for improving predictive models in reactive transport studies.

Understanding how mineral dissolution, precipitation, and gas exsolution interact under reactive flow conditions remains largely unexplored, particularly at the microscale where transient saturation states and confinement effects can drive unexpected phase behavior. It is important to decipher parameters that govern in situ CO_2 generation and entrapment, the microscopic mechanisms of gas exsolution, and the role of solid–fluid interfacial dynamics in modulating mineral transformations. To address these challenges, we developed a novel microfluidic platform (Poonoosamy et al., 2024; Poonoosamy et al., 2021; Poonoosamy et al., 2023) that enables real-time visualization of coupled barite precipitation and CO_2 exsolution during witherite dissolution in acidic, sulfate-rich solutions, to evaluate whether the produced gas dissolves, becomes trapped within the newly formed secondary minerals, or is instead transported with the surrounding fluid. Using optical microscopy, 3D Raman imaging, and geochemical modeling, we explore the effects of pH, sulfate concentration, flow rate, and solid-to-liquid ratios on coupled mineral precipitation and dissolution with gas exsolution.

2. Methods

2.1. Microfluidic experimental setup

The experimental setup consisted of a microfluidic reactor (Fig. 1a) connected to syringe pumps (PHD ULTRA™ Syringe Pumps, Harvard Apparatus, Massachusetts, USA) and monitored using time-lapse optical microscopy. The microfluidic reactor, fabricated out of polymethylmethacrylate (PMMA), consisted of three inlets and three outlets, with dimensions as shown in Fig. 1a. The inlets (mini Luer) of the chip were connected to the pump using Tygon tubing (AAD04103, ID 0.51 mm, OD 1.53 mm, Saint-Gobain Performance Plastics, Akron, OH, USA) using mini Luer connectors (chipshop GmbH, Jena, Germany). The outlet was connected to an effluent vessel.

2.2. Chemical reactions

In our study, we selected a model system in which witherite dissolves under acidic conditions, followed by barite precipitation. This setup provides a simple and controllable chemical environment at ambient temperature and pressure, allowing us to generate gas and investigate its fate during coupled mineral dissolution and precipitation. The solutions used in the experiments include barium chloride ($BaCl_2$) prepared from $BaCl_2{\cdot}2H_2O$ salt > 99 % (index no. 056–004-00–8 Sigma Aldrich), sodium carbonate (Na_2CO_3) prepared from Na_2CO_3 salt > 99.9 % (Merk Cas no. 497–19-8) and sodium sulfate (Na_2SO_4) prepared from Na_2SO_4 salt > 99 % (Cas no. 7757–82-6).

The experiment involved two steps:

(i) Step 1: controlled growth of witherite. In this step, the three inlets (1, 2, and 3) were connected to three 5 mL glass syringes, dispensing solutions of 10 mM $BaCl_2$, deionized water, and 10 mM Na_2CO_3 (Fig. 1a). The outlets directed the effluent into collection vessels. Initially, the microfluidic reactor was filled with deionized water, followed by the injection of the three solutions at a flow rate of 2 μL min^{-1} for 40 min. The introduction of water between the $BaCl_2$ and Na_2CO_3 streams enabled laminar, diffusion-controlled mixing at the interface, enabling the formation of witherite crystals. Despite rigorous measures to maintain reproducibility at this step, flow instabilities arising from the syringe pump can result in crystals exhibiting variable morphologies.

(ii) Step 2: injection of acid and sulfate rich solution. Inlets 1 and 3, as well as outlets 1 and 3, were disconnected and sealed with mini Luer plugs (chipshop GmbH, Jena, Germany). A reactive solution of Na_2SO_4 in hydrochloric acid (HCl) was injected through inlet 2 at defined flow rates.

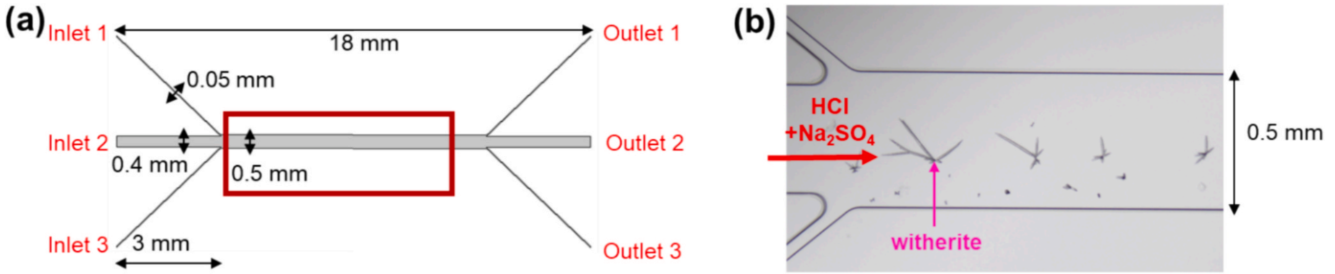

Fig. 1. (a) Microfluidic chip of 10 μm depth, with the red box showing the monitored region, (b) optical micrograph of the microfluidic chip with initially synthesized witherite in Step 1, followed by the injection of a mixed HCl and Na_2SO_4 solution injection during Step 2.

Table 1
Summary of conducted Experiments A–G, along with their corresponding boundary conditions. Details for the estimated rate of dissolution and saturation indices (SI) of all the experiments are given in Supplementary Information S1.

Exp.	pH	Conc. HCl	Conc. Na_2SO_4	Solid volumetric fraction	Flow rates	Velocity u	Dissolution rate of witherite $\frac{r_{diss.}}{A}$	SA $BaCO_3$	SI. barite	Precipitation rate of barite $\frac{r_{precip.}}{A}$	SA $BaSO_4$	Gas observed
		[mol L^{-1}]	[mol L^{-1}]	$(1\text{-}\varepsilon_{H2O})$	[nL min^{-1}]	[m s^{-1}]	[mol m^{-2} s^{-1}]	[m^{2}m^{-3}]		[mol m^{-2} s^{-1}]	[m^{2}m^{-3}]	
A	1	0.1	0.3	0.05–0.25	300	1×10^{-3}	3.2×10^{-5}	46,533	3.6	2.5×10^{-4}	68,725	yes
B	0.2	1	0.3	0.05–0.25	300	1×10^{-3}	3.2×10^{-4}	46,533	4.1	1.9×10^{-3}	68,725	yes
C	2	0.01	0.3	0.05–0.25	300	1×10^{-3}	3.2×10^{-6}	46,533	2.6	2.8×10^{-6}	68,725	no
D	1	0.1	0.1	0.05–0.25	300	1×10^{-3}	3.2×10^{-5}	46,533	3.5	1.5×10^{-4}	68,725	yes
E	1	0.1	0.01	0.05–0.25	300	1×10^{-3}	3.2×10^{-5}	46,533	2.8	6.7×10^{-6}	68,725	no
F	1	0.1	0.3	0.05–0.25	1000	3.3×10^{-3}	1.3×10^{-3}	46,533	4.7	3.5×10^{-2}	68,725	yes
G	1	0.1	0.3	0.5–0.80	300	1×10^{-3}	3.2×10^{-5}	9,432,976	6.0	1.3×10^{-1}	68,725	yes

The injection of an acidic solution is expected to initiate the dissolution of witherite (Equation 1), releasing barium ions ($Ba^{2+}_{(aq)}$), which would subsequently react with sulfate ions ($SO^{2-}_{4(aq)}$) from the inflowing solution, leading to the precipitation of barite ($BaSO_{4(s)}$) (Equation 2). Simultaneously, the aqueous CO_2 ($CO_{2(aq)}$) generated during dissolution would equilibrate with the solution and could be exsolved as gas (Equation 3).

$$BaCO_{3(s)} + 2H_3O^+_{(aq)} \leftrightarrow Ba^{2+}_{(aq)} + 2H_2O_{(l)} + H_2CO_{3(aq)} \tag{1}$$

$$Ba^{2+}_{(aq)} + SO^{2-}_{4(aq)} \leftrightarrow BaSO_{4(s)} \tag{2}$$

$$H_2CO_{3(aq)} = H_2O, CO_{2(aq)} \leftrightarrow CO_{2(g)} + H_2O_{(aq)} \tag{3}$$

Seven experiments (labeled A to G) were conducted with varying flow rates, pH levels, Na_2SO_4 concentrations and volumetric solid fractions (Table 1). The pH acid used in our experiments were ≤ 2. Such low-pH conditions, though rare in most subsurface environments, can occur in acid mine drainage systems with pyrite oxidation ((Becking et al., 1960; Nordstrom et al., 2000), in engineered settings such as passive limestone drains or acid stimulation during hydraulic fracturing, where carbonate buffering and localized CO_2 degassing may influence secondary sulfate precipitation. All experiments were performed at ambient temperature (21 °C) and pressure.

2.3. *Optical microscopy imaging*

Imaging was conducted using an inverted Nikon Eclipse Ti2 microscope (Nikon, Tokyo), equipped with a motorized stage. Images for Experiments A–F were acquired using a 100 × oil immersion objective (CFI Plan Apochromat, NA 1.45, refractive index 1.515, Nikon, Tokyo), while a 40 × objective (CFI Plan Apochromat, NA 0.95, Nikon, Tokyo) was used in Experiment G to capture a larger field of view. High-resolution micrographs (170 μm × 170 μm) were collected in differential interference contrast (DIC) mode using a Zyla sCMOS camera (Andor, Belfast) for Experiments A–F. Image acquisition was performed at 10 positions within a 10 mm monitored region (Fig. 1), at regular intervals of 20 to 30 s, depending on the dynamics of the observed reactions. In Experiment G, micrographs with a 436 μm × 436 μm field of view were captured to accommodate additional processes that emerged during the experiment.

2.4. *Raman 2D and 3D imaging*

Experiment A was repeated using real-time Raman spectroscopy to analyze both solid material and encrusted bubbles. Due to laser power limitations, gas-phase tracking was not feasible. Measurements were conducted using a Witec alpha300 Ri Inverted Confocal Raman Microscope, equipped with a Nikon 100 × oil immersion objective (NA = 1.4, working distance = 0.13 mm, with cover glass correction). The system employed a 70 mW Nd:YAG laser (λ = 532 nm), operated at 13.6 mW – the maximum achievable with the current laser condition. The theoretical diffraction-limited lateral and axial resolutions of the Raman measurements at the sample surface were ~ 464 nm and ~ 629 nm, respectively, based on Equation (3) and (4) in Everall (Everall, 2008), considering the refractive index of the immersion medium (n = 1.55). A 600 grooves per mm grating provided a spectral resolution of 4 cm^{-1}, and a thermoelectrically cooled CCD detector was used for signal acquisition. Raman intensities for 2D depth mapping were collected with a 0.3 s integration time over the 500–3800 cm^{-1} wavenumber range.

At the end of all experiments (A – G), 3D Raman imaging was performed at a minimum of two locations per experiment. Scans were conducted with a step size of 500 nm in the x and y directions and 1 μm in the z direction over a depth of 10 μm. Raman intensities were recorded with an integration time of 0.1 s across the 300–1400 cm^{-1}

wavenumber range. A grating with 1800 grooves per mm providing a spectral resolution of 1 cm^{-1} was used for these measurements. These 3D datasets enabled single-crystal analysis to quantify mineral dissolution and precipitation. Image stacks were processed and visualized using ImageJ 3D Viewer (version 4.0.2).

2.5. *Image analysis of microfluidic experiments*

Due to the similar grayscale intensities of gas bubbles and crystals in DIC images, automated segmentation algorithms failed. Therefore, manual segmentation was performed using a paint-style application to annotate regions of interest based on morphological features (Santoso et al., 2025): bubbles were identified by their rounded shapes, while crystals showed angular edges and faceted outlines. These visual distinctions are easily recognizable to the human eye, even when grayscale intensities overlap. The areas of the growing bubbles and initial crystals of the segmented images were evaluated for different time steps. Both the original and segmented images are available in the data repository.

2.6. *Transport control versus reaction control process*

The dissolution of witherite with time [mol s^{-1}] in an acidic sulfate-rich solution follows:

$$r_{diss.} = \frac{-dn_{witherite}}{dt} = -A \times k_{diss.}\{a_{H^+}\}(1 - \Omega_{witherite}) \tag{4}$$

where A [m^2] is the reactive surface area of witherite, $k_{diss.}$ [mol m^{-2} s^{-1}] is the acidic dissolution rate constant (0.76mol m^{-2} s^{-1}at 298.15 K; (Chou et al., 1989)), $\{a_{H^+}\}$ is the activity of H^+, and $\Omega_{witherite}$ is the saturation state of the solution which remains significantly $\ll 1$ under far-from-equilibrium conditions as in our experiments.

Two additional experiments were conducted to measure the dissolution rate of witherite in the microfluidic configuration at two different flow rates: 300 and 1000 nL min^{-1}. An HCl solution (pH 1) was injected into a microfluidic channel containing witherite at a volumetric solid fraction of 0.11 (i.e. 1-εH_2O = 0.11). The dissolution rates of witherite at pH 1, $\frac{r_{diss.}}{A}$ [mol m^{-2} s^{-1}], in the microfluidic reactor were measured at (3.2 ± 0.1) × 10^{-5} mol m^{-2} s^{-1} and (1.3 ± 0.3) × 10^{-3} mol m^{-2} s^{-1} for flow rates of 300 nL min^{-1} and 1000 nL min^{-1}, respectively (Table 1). The dissolution rates for Experiments B (pH 0.2) and C (pH 2) were estimated as function of pH as rate of dissolution is proportional to $\{a_{H^+}\}$ (Equation 4).

The reactive surface area for witherite is calculated from the specific surface area, SA [m^2 m^{-3}] evaluated from images as the area exposed to the fluid (perimeter of crystal × depth of reactor) per unit volume and is reported for each experiment in Table 1.

The rate of barite precipitation follows (Bosbach, 2002):

$$r_{precip.} = \frac{dn_{barite}}{dt} = A \times k_{precip.}(1 - \Omega_{barite})^2 \tag{5}$$

with $k_{precip.}$ equal to 1.5 × 10^{-11} $molm^{-2}s^{-1}$ and where the saturation state of barite (Ω_{barite}) is given by:

$$\Omega_{barite} = \frac{\{aBa^{2+}\}\{aSO_4{}^{2-}\}}{K_{sp(barite)}} \tag{6}$$

where $K_{sp(barite)}$ is the solubility product of barite equal to $10^{-9.97}$ mol^2 L^{-2} at 298.15 K (Hummel et al., 2002; Thoenen et al., 2013), and $\{aBa^{2+}\}$ and $\{aSO_4{}^{2-}\}$ are the activities of Ba^{2+} and SO_4^{2-}, respectively. The reactive surface area of barite is calculated from the specific surface area, SA [m^2 m^{-3}], evaluated from images as the total area occupied by newly formed precipitate per unit volume and considered the same for all experiments (Table 1).

Table 2

Analysis of transport versus reaction in Experiments A-G. Pe denotes Peclet number, $Da_{I(BaCO_3)}$, $Da_{II(BaCO_3)}$ denotes the Damköhler number of the first and second kind based on witherite dissolution; $Da_{I(BaSO_4)}$ and $Da_{II(BaSO_4)}$ denotes the Damköhler number of the first and second kind respectively based on barite precipitation. (N.B the ratio of the Da is the same whether the first or second kind is used).

Exp.	Pe	$Da_{I(BaCO_3)}$	$Da_{I(BaSO_4)}$	$Da_{II(BaCO_3)}$	$Da_{II(BaSO_4)}$	$\frac{Da_{BaSO_4}}{Da_{BaCO_3}}$
A	170	4	2.8×10^2	6.1×10^2	4.8×10^4	78
B	170	36	2.1×10^3	6.1×10^3	3.6×10^5	60
C	170	0.4	3.2×10^1	6.1×10^1	5.4×10^2	9
D	170	4	1.64×10^2	6.1×10^2	2.8×10^4	46
E	170	4	7.5×10^1	6.1×10^2	1.3×10^3	2
F	567	43	1.2×10^4	2.4×10^4	6.8×10^6	281
G	170	726	1.4×10^7	1.2×10^5	2.4×10^9	19,699

To estimate the local saturation state, the saturation index (SI) of barite, and the precipitation rate of barite, the concentration of aqueous $Ba^{2+}_{(aq)}$ [mol m^{-3}] around the witherite crystals was calculated using the following equation:

$$\left[Ba^{2+}_{(aq)}\right] = -\frac{r_{diss.}}{V(\varepsilon H2O)} \times \frac{\Delta x}{u} \tag{7}$$

where Δx is the length of the monitored FOV (170 μm) and u is the velocity of the fluid equal to 1 × 10^{-3} m s^{-1} and 3.33 × 10^{-3} m s^{-1} for experiments conducted at flow rates of 300 nL min^{-1} and 1000 nL min^{-1}, respectively. V is the volume of FOV equal to 2.89 × 10^{-13} m^3 (170 μm × 170 μm × 10 μm). The solid fraction (1-εH_2O) of Experiment A-F were set to 0.11 while that of Experiment G was set to 0.6. The activities were computed using GEMs selector based on the concentrations. The concentration of SO_4^{2-} is that of the injected sodium sulfate solution. The concentration of Ba^{2+} was obtained by conducting additional dissolution experiments (see Supplementary Information S1) and measuring the amount of witherite that has dissolved within the field of view with time. The SI with respect to barite varies between 2.8 and 6, a relatively high SI, which, however, can prevail in geothermal brines of hydrothermal vent systems at mid oceans ridges (Jamieson et al., 2016).

In addition, the Peclet and Damköhler numbers were also calculated as part of our analysis (Table 2). The Peclet number quantifies the relative influence of advection versus diffusion in solute transport and is defined as (Sanchez-Vila et al., 2010; Steefel and Maher, 2009):

$$Pe = \frac{uL}{D} \tag{7}$$

where u denotes the velocity [m s^{-1}], L [m] denotes the characteristic length scale (170 μm field of view), and D denotes the diffusivity. When $Pe > 1$, advection dominates; conversely, $Pe < 1$ indicates diffusion-dominated transport (Sanchez-Vila et al., 2010; Steefel and Maher, 2009). As shown in Table 2, all experiments exhibit Peclet numbers greater than one, indicating advection-dominated conditions.

The metric to describe the interplay of transport and reaction is the Damköhler number of the first kind Da_I (Salehikhoo et al., 2013; Sanchez-Vila et al., 2010; Steefel and Maher, 2009). For the evaluation of our experiments where both dissolution and precipitation occurred, we define two separate Damköhler numbers:

1. For witherite dissolution:

$$Da_{I(BaCO_2)} = \frac{r_{diss.L}}{Vu \times C_{eq}^{Ba^{2+}}} \tag{8}$$

2. For barite precipitation:

$$Da_{I(BaSO_4)} = \frac{r_{precip.L}}{Vu \times C_{eq}^{Ba^{2+}}} \tag{9}$$

where C_{eq} [mol m^{-3}] denotes the equilibrium concentration equal to 7.12×10^{-2} mol m^{-3}, 1.04×10^{-2} mol m^{-3} for equation 8 and 9 respectively

The system can also exhibit flow heterogeneities where diffusion might be the controlling transport mechanism of solutes and consequently the Damköhler numbers of the second kind (Da_{II}) which consider diffusive transport, computed here for completeness, are given as:

1. For witherite dissolution:

$$Da_{II(BaCO_2)} = \frac{r_{diss.}L^2}{\nu D \times C_{eq}^{Ba^{2+}}} \tag{10}$$

2. For barite precipitation:

$$Da_{II(BaSO_4)} = \frac{r_{precip.}L^2}{\nu D \times C_{eq}^{Ba^{2+}}} \tag{11}$$

Da > 1 indicates fast reaction and that the process is transport-controlled, while Da < 1 indicates a slow reaction, and the process is reaction-controlled. Together, Pe and Da numbers provide insight into whether the observed dynamics are governed primarily by transport or reaction kinetics.

2.7. Setup of geochemical model using GEMS

The GEM2MT flow through simulation module of GEMS (Gibbs Energy Minimization Software) (Kulik et al., 2013) was used to simulate a simplified reactive fluid flow through a rock column over a number of time steps. Rather than serving for direct comparison with our experiments, the objective of these simulations was to determine under which acid concentration gas would be exsolved and transported in the system. The thermodynamic properties of solids (barite and witherite), aqueous species and gases in the chemical system are based on the PSI/Nagra thermodynamic database 12/07 (Thoenen et al., 2013). The gas phase was modeled as a multi-component fluid (CO, CO_2, H_2, H_2O, O_2) using the Peng-Robinson-Stryjek-Vera cubic equation of state ideal mixing of these gas components (Peng and Robinson, 1976; Stryjek and Vera, 1986).

For the geochemical model, a chemical system was defined consisting of barite, witherite, and mixed HCl/Na_2SO_4 solution. A flow-through reactor chain was constructed out of 100 units (reactors or boxes), through which an acidic sulfate-containing solution is transported (Fig. 2). The witherite units (boxes 2 to 99) are made out of witherite solid. The solid volumetric fraction was fixed to 0.05 initially, $1 - \varepsilon H_2O = 0.05$. The aqueous solutions used in Experiments A-E were considered as boundary conditions defined in box 1, acting as infinite source of solution with constant composition. At each step, 10 wt% of the aqueous solution from each box moves and reacts in the next box in the chain, continuing until box 100, which acts as an infinite sink boundary. No kinetic rate laws were applied in the GEMS simulation; each step represents equilibrium advancement rather than a real-time interval. This approach approximates fluid movement under steady-state conditions. After a given number of steps, the propagation of alteration zones and reaction front were followed by plotting the amounts of phases and components in all boxes.

3. Results

3.1. Coupled mineral dissolution and precipitation with gas exsolution

A microfluidic experiment was designed to investigate coupled mineral dissolution and precipitation with gas exsolution. The experiment involved injecting a reactive acidic sodium sulfate solution into a microfluidic reactor (Fig. 1a) containing witherite ($BaCO_3$) crystals.

Under controlled conditions (flow rate: 300 nL min^{-1}, 0.3 M Na_2SO_4 solution at pH 1, and a volumetric solid fraction of 0.05–0.25 (within different regions of interest in the microfluidic channel), referred to as Experiment A in Table 1), witherite dissolution became evident within four minutes, initiating with the disruption of the crystals in some cases (red boxes in Fig. 3). Within 12 min, gas bubbles formed, coated with a barite layer (Fig. 3), leading to a "cauliflower- like structure", where CO_2 bubbles grew with barite precipitating on their surface (Movie 1). As the bubbles grew, their initially rounded shape was progressively altered by the combined effects of barite growth guided by its crystallography and the directional flow of the solution. At later stages of the experiment, dissolution was still taking place. Consequently gas, appearing after 80 min as dark patches indicated by black arrows in Fig. 3, moved withing the encrusted witherite crystals trying to get out (Movie 2). This rapid movement of gas bubbles back and forth in the crystals appeared similar to self-propelled droplet movement in conical structures (Liu et al., 2022; Lv et al., 2014; McCarthy et al., 2019).

To ensure reproducibility, the experiment was duplicated, with in situ Raman spectroscopy measurements recorded (Fig. 4). Gas bubbles were systematically analyzed during their formation (Fig. 4), and Raman spectra revealed an unexpected presence of water (liquid) within the bubbles, though at a lower intensity as compared to the surrounding solution outside the bubble (Fig. 4c). The water present is most likely in the form of fine droplets evenly dispersed like a cloud and not as a dense liquid at the bottom of the bubble. $CO_{2(g)}$ is not detected in our measurement because of the low laser intensity of our instrument.

To quantify the role of acidity and saturation index on the growth of encrusted bubbles, we evaluated the ratio of the area occupied by the encrusted bubble to the area initially occupied by the witherite crystal (A(t)/A(t = 0)), and plotted this ratio over time (Fig. 5a). In Experiment

Fig. 2. Schematic of the flow-through reactor chain model implemented in the GEMS Selektor geochemical solver, where a continuous flux of fluid is pumped into the first witherite unit and subsequently passes through each successive unit.

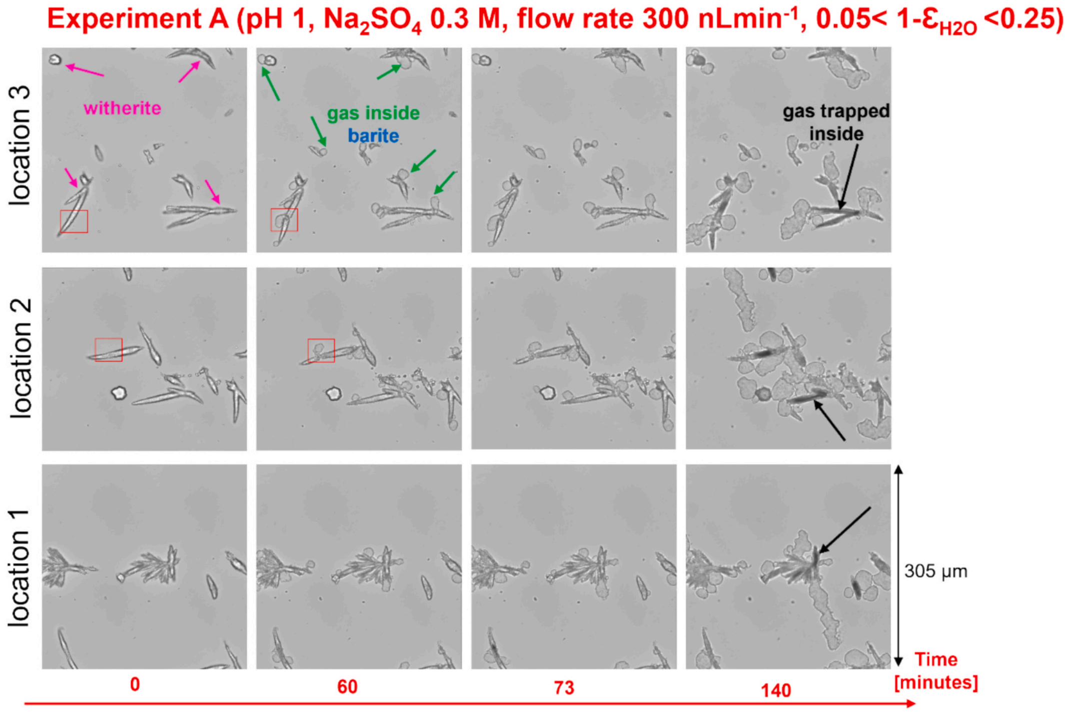

Fig. 3. Microfluidic experimental results of reference case study, Experiment A. Optical micrographs of different sampled locations with time showing pristine witherite crystals (pink arrows), dissolution and crystals breaking apart (red boxes), growing gas bubbles encrusted in barite (green arrows), and gas movement within the original crystal (black arrows). Locations 2 and 3 demonstrate the reproducibility of the process.

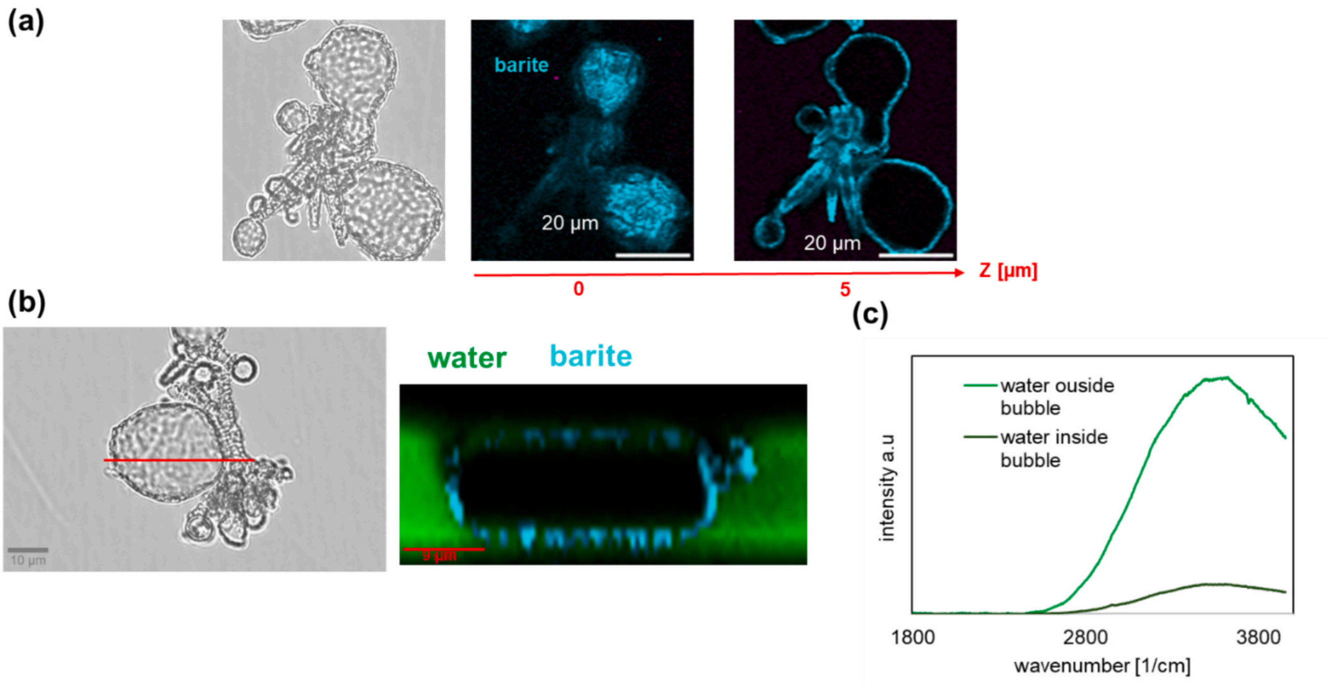

Fig. 4. Raman analysis of Experiment A. (a) sampled locations with optical micrographs and associated Raman imaging across the depth of the reactor, with z = 0 µm at the bottom of the reactor and z = 5 µm at the middle of the reactor, showing that barite (cyan blue) has completely replaced witherite and forms a crust around gas bubbles after two hours. (b) Raman imaging depth scan (right) performed perpendicular to the view in the photo on the left (along red line). (c) Raman signal intensity measured inside and outside the bubble from e capturing the water bands after 40 min.

A, this ratio increased from 0 to a maximum value of 1.5 within 140 min. Multiple locations with slightly varying initial volumetric solid fraction (1-εH_2O), defined by the area initially occupied by pristine witherite in the field of view of 170 µ m × 170 µm, were analyzed, all yielding similar results (Fig. 5a).

3.1.1. *Effect of pH*

In Experiment B, where a pH 0.2 solution was injected, gas bubbles encapsulated by a barite layer appeared within just two minutes. Unlike in Experiment A, the gas bubbles did not retain a rounded morphology but instead formed angular, irregular shapes, rapidly evolving into

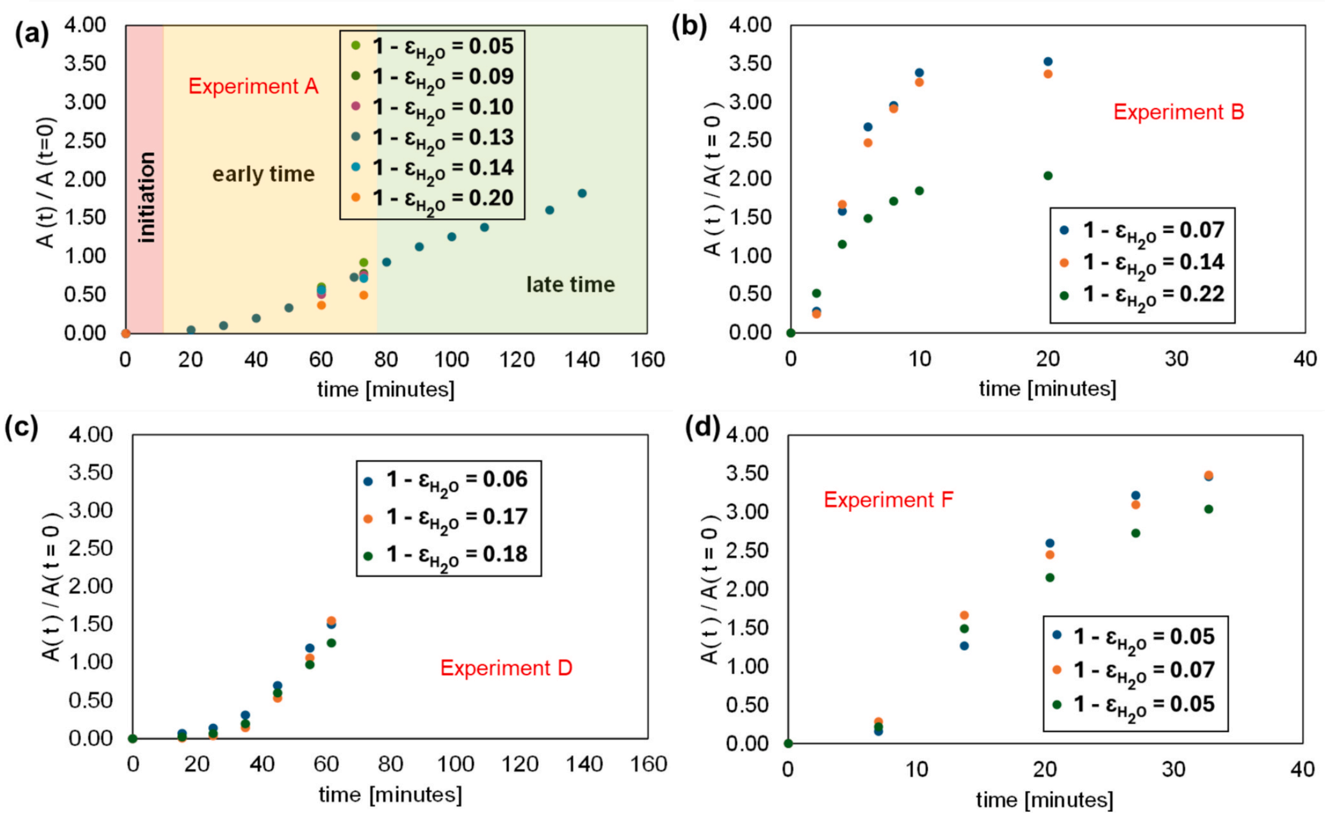

Fig. 5. A measure of the "cauliflower-like structures" for comparing the experiments. Graphs showing the ratio of the area occupied by the gas bubbles encrusted within barite (A(t)) to the area occupied by the initial witherite crystal (A(t = 0)) over time for Experiments A, B, D, and F, respectively with $1 - \varepsilon H_2O$ the volumetric initial witherite fraction the FOV. For Experiments C and E, A(t) = 0. The error associated with the ratio A(t)/A(t = 0) is 0.46 % estimated from the pixels along the perimeter and in the area, while the error for the time is ± 20 s. Both of these errors are small and therefore do not appear in the graphs.

interconnected structures that bridged multiple bubbles (Fig. 6a, Movie 3). This reaction ultimately led to the complete replacement of witherite by barite, as confirmed by Raman imaging (Fig. 6b). The ratio of A(t)/A (t = 0) increases to 3.5 within 20 min (Fig. 4b), much faster than in Experiment A. A small increase in the initial volumetric solid fraction ($1 - \varepsilon H_2O = 0.22$) also led to a lower ratio of the area of the bubbles to the area of the crystals (Fig. 5b), because the bubbles had less space available to expand in this particular configuration.

In contrast, when a pH 2 solution was injected (Experiment C), no gas formation was observed (Fig. 6c, Movie 4). Instead, dissolution occurred, followed by barite precipitation starting as "ridges" on the surface of witherite. Over time, barite precipitates accumulated, forming an armoring layer that shielded the remaining witherite (Fig. 6d) from further dissolution, leading to complete passivation within one hour. The average conversion of witherite to barite was estimated from our 3D Raman image as 63.0 ± 0.1 %.

3.1.2. *Effect of saturation with respect to barite*

The local saturation index (SI), as calculated in supplement S1, with respect to barite is influenced by the conditions near witherite surfaces, the fluid injection rate, and sulfate concentration in solution as well as the pH of the injected solution which releases aqueous barium. This section evaluates the effect of sulfate concentration while maintaining constant flow rates and pH. Our observations indicate that a saturation index of 3.5 leads to the "cauliflower-like structures" (Fig. 7a) in Experiment D, whereas this phenomenon is absent at a lower SI of 2.8 (Fig. 7b) in Experiment E. In Experiment E, we observe a dissolution of witherite followed by the precipitation of tiny crystals of barite. A comparison between Experiment A (0.3 M Na_2SO_4, SI = 3.6) and Experiment D (0.1 M Na_2SO_4, SI = 3.5) reveals that the encrusted structures in Experiment D exhibit fewer bubble-like features but share greater morphological similarity with those observed in Experiment B. The ratio of A(t)/A(t = 0) in Experiment D increases to 1.5 within 60 min (Fig. 5c) faster than in Experiment A.

3.1.3. *Effect of flow rates*

Increasing the flow rate from 300 to 1000 nL min^{-1} results in a measurable increase in the dissolution rate of witherite by one order of magnitude (see Supplementary Information S1). In Experiment F, where the flow rate is higher than in Experiment A, the "cauliflower-like structures" are also observed (Fig. 6c). However, unlike Experiment A, bubble formation occurs much faster with A(t)/A(t = 0) = 3.5 after 35 min (Fig. 5d).

3.1.4. *Effect of volumetric solid fraction*

In Experiment G, the volumetric solid fraction was increased by allowing witherite crystals to grow for more than one hour in step 1 (cf. Methods section). This resulted in the formation of dendrite-like structures, as shown in Fig. 8. The "cauliflower-like structures" were observed, along with the formation of free (not trapped) gas bubbles that grew over time (Movie 5). CO_2 bubbles were either trapped within the dendritic structures (ganglia) or transported along with the flow, transitioning the system from single-phase (liquid) to two-phase (gas–liquid) flow (Fig. 8a and b). Indeed, in some locations the dissolved aqueous CO_2 reached supersaturation such that exsolution was possible forming gas bubbles that grew with time. The encrusted barite layer also seems to shield the primary mineral, preventing further dissolution, as evidenced by 3D Raman analysis (Fig. 8c). 3D Raman imaging at two locations indicated a 76 % conversion of witherite to barite. Due to the complexity of the dendritic structures, accurately segmenting the image to quantify the gas phase was challenging. Nevertheless, it appears that encrusted bubbles occupy all available spaces between the dendrites. At later

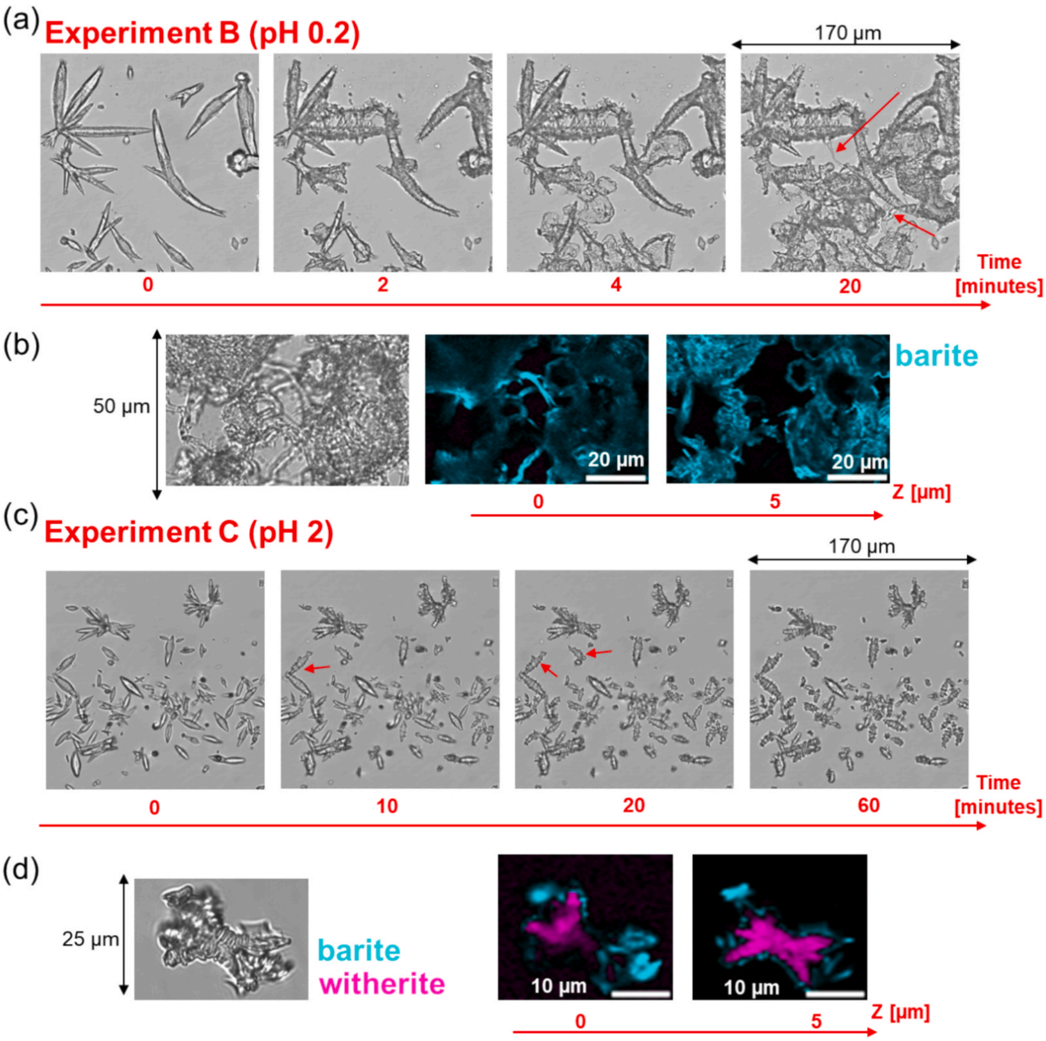

Fig. 6. Combined optical microscopy and Raman analyses of Experiments B–C. (a) Optical micrograph showing witherite dissolution with rapid gas production and barite precipitation over time. Red arrows at t = 20 min indicate capillary bridges in Experiment B. (b) Illustrative Raman images of the alteration, where barite (cyan blue) has completely replaced witherite. (c) Optical micrograph of coupled witherite dissolution and barite precipitation in Experiment C. (d) Illustrative Raman images of the alteration, where barite (cyan blue) coats witherite (pink).

stages the precipitated barite exhibited a morphology distinct from those observed in our previous experiments in some locations. Instead of forming encrustations on bubbles or on mineral surfaces, this phase appeared to precipitate rapidly within free spaces (indicated by yellow arrows in Fig. 8b, Movie 6). The high solid volumetric fraction likely contributed to a localized high saturation index (SI) with respect to barite, as shown in Table 1, due to enhanced dissolution leading to a homogeneous nucleation of barite (yellow arrows in Fig. 8b). Morphologically, this barite phase resembled the nanocrystalline structures associated with homogeneous nucleation under high SI conditions, as previously reported (Poonoosamy et al., 2016) and also appear extinct under crossed polarized light. Further analysis is necessary to confirm this similarity.

3.2. Geochemical modelling

To evaluate how the coupled dissolution of witherite under acidic conditions and precipitation of barite influence CO_2 production and, consequently, the observed “cauliflower-like structures”, we conducted a simplified geochemical simulation. This modeling work did not directly replicate our experiments as only equilibrium calculations were considered (i.e. no kinetics) – since, to our knowledge, no existing reactive transport code can fully handle such processes – but instead served as a tool for process comprehension.

According to our model, a solution with pH 1 containing 0.3 M Na_2SO_4 (Experiment A) promotes the dissolution of witherite, releasing gaseous CO_2 (Fig. 9a) along with water vapor ($H_2O_{(g)}$) (Fig. 9b). This leads to the formation of both a dissolution front (Fig. 9c) and a precipitation front (Fig. 9d). Only the major carbonate species are presented here, and the production of water vapor and CO_2 gas are correlated, as indicated by similar graph trends.

Injecting a solution with pH 0.2 (Experiment B) results in higher CO_2 and water vapor production, as well as a greater advancement of both the dissolution and precipitation fronts. This solution also dissolves more witherite per unit of witherite and per flux in each time step leading to greater flux of Ba^{2+} than available SO_4^{2-}, resulting in more dissolution than precipitation per unit of witherite. Conversely, using a solution with pH 2 (Experiment C) does not generate significant gaseous CO_2 or water vapor, though the dissolution and precipitation behavior remains similar to that observed in the simulated Experiment A.

Reducing the Na_2SO_4 concentration to 0.1 M (Experiment D) or 0.01 M (Experiment E) leads to localized $CO_{2(g)}$ generation, which subsequently dissolves as the reaction progresses. This results in a slower advancement of both the dissolution and precipitation fronts (Fig. 9c and d).

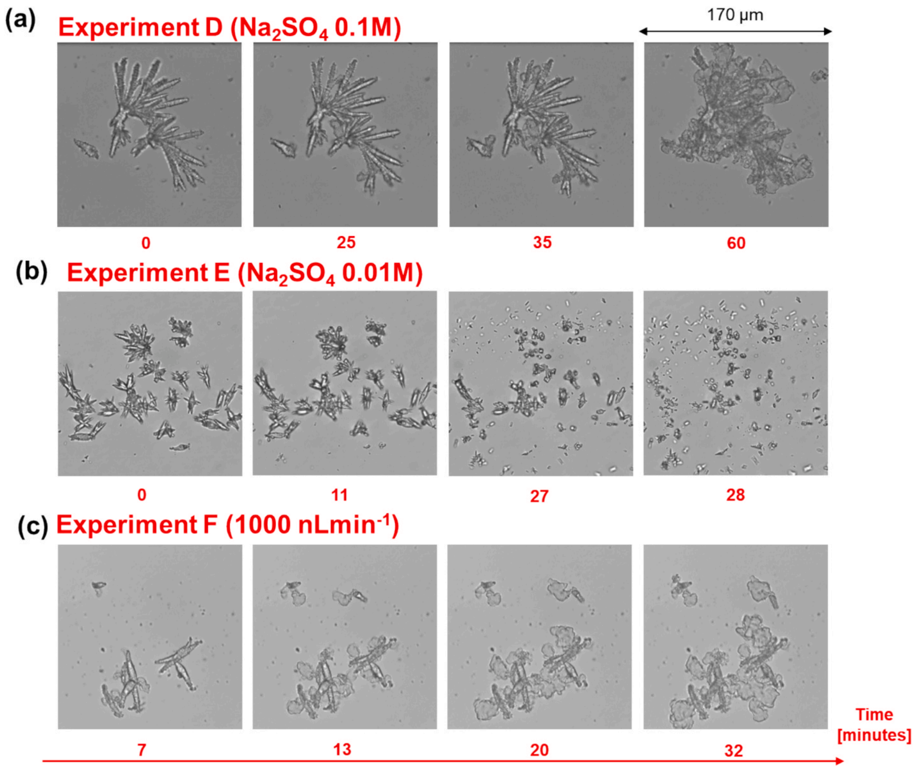

Fig. 7. Optical micrographs of the temporal evolution of Experiments D, E, and F. (a) Micrographs showing the “cauliflower-like structures” in Experiment D. (b) Micrographs showing predominant dissolution of witherite crystals without gas exsolution and the precipitation of tiny barite crystals in Experiment E. (c) Micrographs showing the “cauliflower-like structures” observed in Experiment F.

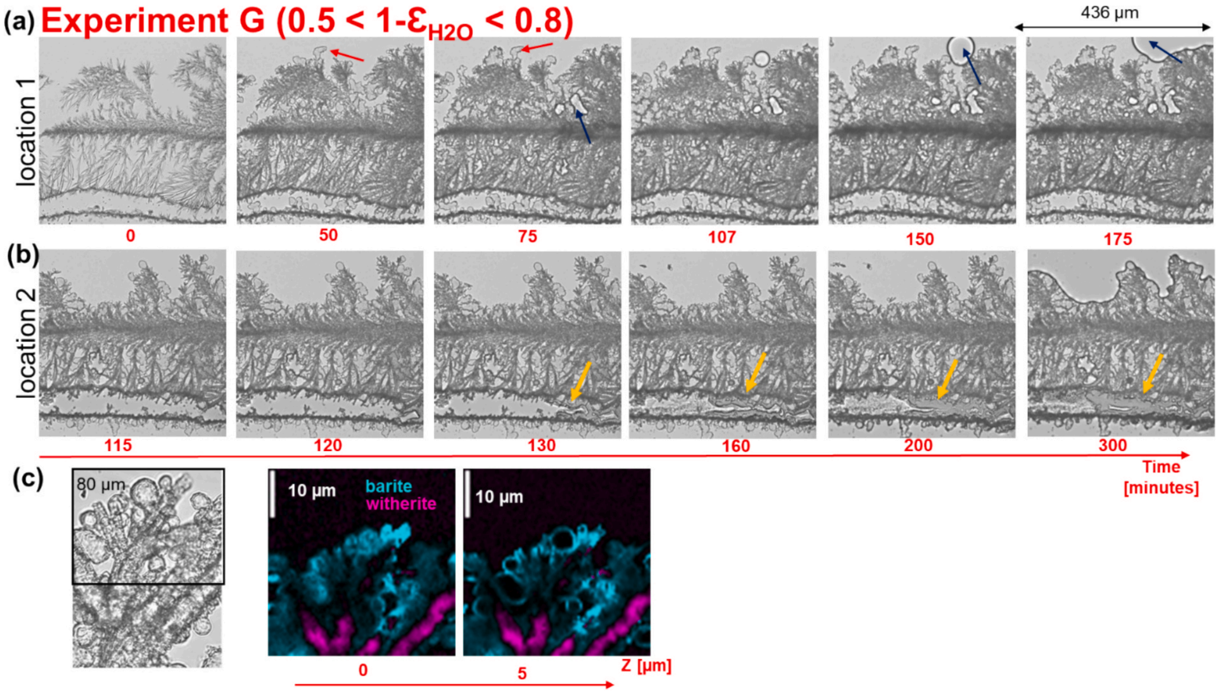

Fig. 8. Optical micrograph at location 1 in Experiment G. (a) Shows the formation of barite-encrusted bubbles that shield the primary witherite from dissolution, along with the formation of free gas bubbles, that can grow (blue arrows) and/or move with the flow. (b) Optical micrograph at location 2 in Experiment G with yellow arrows indicating the precipitation of homogeneous barite not encrusting gas bubbles. (c) Raman imaging illustrating unreacted primary witherite shielded by barite precipitation in Experiment G.

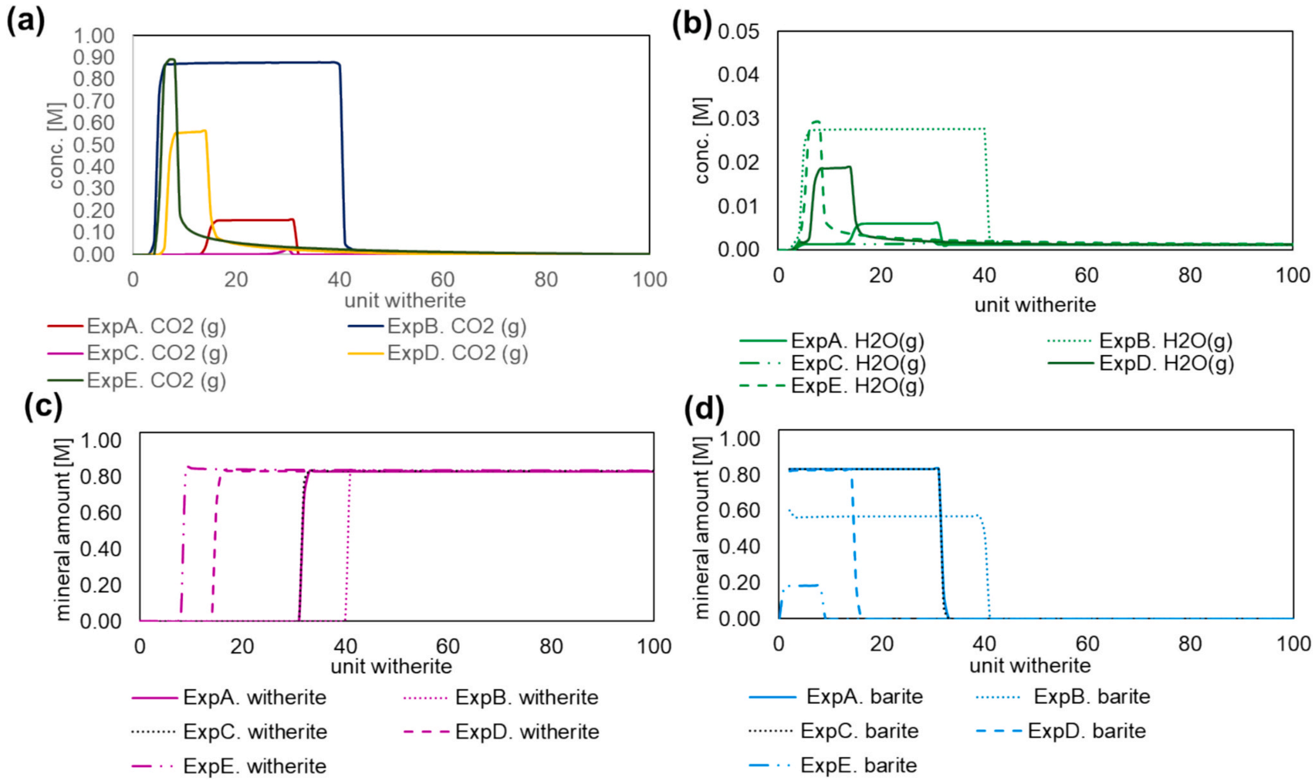

Fig. 9. Geochemical modelling results after 1000-time steps. (a-d) Simulated evolution of key geochemical parameters along the 100-unit witherite flow chain, considering the boundary conditions (acid and sulfate concentrations) from Experiments A – E: (a) CO_2 gas; (b) water vapor; (c) Amount of witherite ($BaCO_3$) and (d) barite ($BaSO_4$) present in the boxes at the end of the numerical experiment.

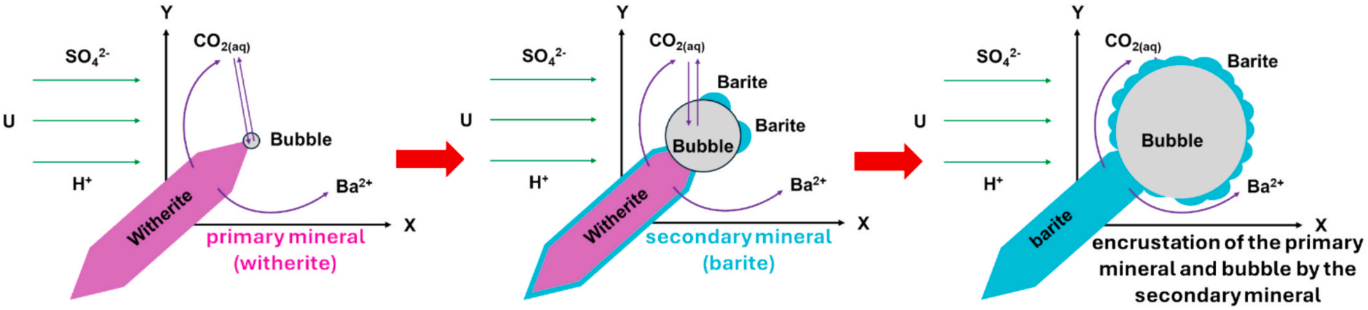

Fig. 10. Schematics of the formation of "cauliflower-like structures".

4. Discussion

4.1. The formation of "cauliflower-like structures": competition between dissolution and precipitation rate

A key finding of this study is the emergence of distinct "cauliflower-like structures", characterized by growing CO_2 bubbles encrusted within a growing barite layer. The different steps of the interface coupled mineral dissolution and precipitation with gas exsolution are depicted in Fig. 10. Barite is formed primarily on the surface of the gas bubbles because of the lower surface tension – compared to the surface tension associated with nucleation in the free solution – promoting its nucleation (Desarnaud et al., 2016; Hulin and Mercury, 2019a, b). The presence of gas bubbles inherently involves the formation of thin water films and, consequently, the development of an electrical double layer (Yang et al., 2024), which increases reactivity at the gas–aqueous interface (Albéric et al., 2018). The electric charge and zeta potential at the surface of CO_2 bubbles may influence the distribution of solutes. Gas bubbles are generally known to have a negative zeta potential and can thus attract positively charged Ba^{2+} ions. This interaction may facilitate the local accumulation of SO_4^{2-} species through charge compensation (Leroy et al., 2012), increasing the saturation index (SI) with respect to barite and thereby promoting its precipitation.

The morphology and dynamics of these bubbles are strongly influenced by pH, sulfate concentration, and flow conditions. The underlying mechanism governing this phenomenon is the competition between the dissolution of witherite ($BaCO_3$) and the precipitation of barite ($BaSO_4$), both of which are dictated by solution chemistry and reaction kinetics.

In Experiment A, the dissolution and precipitation rates are 3.2×10^{-5} and 2.5×10^{-4} mol m^{-2} s^{-1}, respectively, with a ratio of precipitation to dissolution rates equal to 8. At pH = 2, witherite dissolution occurs at a rate of 3.2×10^{-6} mol m^{-2} s^{-1} without significant gas exsolution, leading to the formation of a passivating barite layer at a rate of 2.8×10^{-6} mol m^{-2} s^{-1} that inhibits further reaction. Generally, the "cauliflower-like structures" are also observed in Experiments B, D, F, and G, where the ratio of $BaSO_4$ precipitation rate to $BaCO_3$ dissolution rate exceeds 1 (see Table 1); that is, when precipitation is faster than dissolution. However, explaining the process based solely on reaction kinetics is insufficient; transport effects must also be considered (see next section).

Interestingly, no gas bubbles were observed in Experiment E ($pH = 1$, low sulfate concentration), despite conditions favoring witherite dissolution at similar rates as in Experiment A and D. A possible explanation is that the slow precipitation of barite allows for rapid renewal of the local solution chemistry, preventing aqueous CO_2 supersaturation to reach the threshold for exsolution. When the sulfate concentration increases, the precipitation rate of barite increases and begins to match the dissolution rate of witherite leading to sustained CO_2 production in the vicinity of the witherite and the emergence of the "cauliflower-like structures".

Additionally, the dissolution rate is enhanced at lower pH and higher flow rates, further increasing CO_2 production and the likelihood of encrusted gas bubbles. Increasing the flow rate promotes witherite dissolution, which in turn accelerates CO_2 exsolution and enlarges the cauliflower structures (area of encrusted bubble / area of initial crystal > 3). Furthermore, increasing the solid-to-liquid ratio (Experiment G) to mimic porous media conditions results in excessive CO_2 gas formation and the transition from a single-phase to a two-phase flow regime, where "free" gas bubbles flow through the system. The precipitated barite layer also acts as a protective shield on witherite, limiting further dissolution of witherite and altering the overall reaction dynamics.

A key observation from Raman spectroscopy (Fig. 4c) was the unexpected detection of liquid water within the CO_2 bubbles, despite geochemical models predicting the formation of water vapor. Although the H_2O Raman signal was weaker than the surrounding solution, its presence suggests tiny water droplets (clouds) trapped within the encrusted bubble. This entrapment could result from a combination of capillary forces within the encrusted barite shell and partial water vaporization due to local pressure fluctuations, potentially through capillary condensation (Yang et al., 2020). The formation of clouds is also reported during cavitation phenomena (Reese et al., 2024). The detection of clouds within the bubbles further indicates a dynamic gas-fluid interaction, which could influence bubble stability, growth kinetics, and barite precipitation patterns.

The geochemical simulations indicate that at $pH = 1$, CO_2 is readily produced from witherite dissolution, whereas at $pH \geq 2$, gas generation is negligible, consistent with the absence of bubbles in Experiment C. The modeled CO_2 production is highest in Experiment B, which aligns with the experimentally observed rapid growth of "cauliflower-like structures", reflecting the fast dissolution of witherite. Comparing the modeled results for Experiments A, B, and D, where pH is identical, but Na_2SO_4 concentrations vary, reveals that the dissolution front decreases as sulfate concentrations decrease, highlighting the role of SO_4^{2-} ions in addition to H^+ in driving the disequilibrium of witherite. While the current model does not capture the 'real' transport dynamics, the experiments demonstrate that higher flow rates and volumetric solid fractions enhance dissolution, CO_2 production, and the formation of encrusted structures. Together, these observations indicate that the "cauliflower-like structures" emerge when dissolution-driven CO_2 accumulation exceeds local transport, enabling rapid barite nucleation on bubble surfaces.

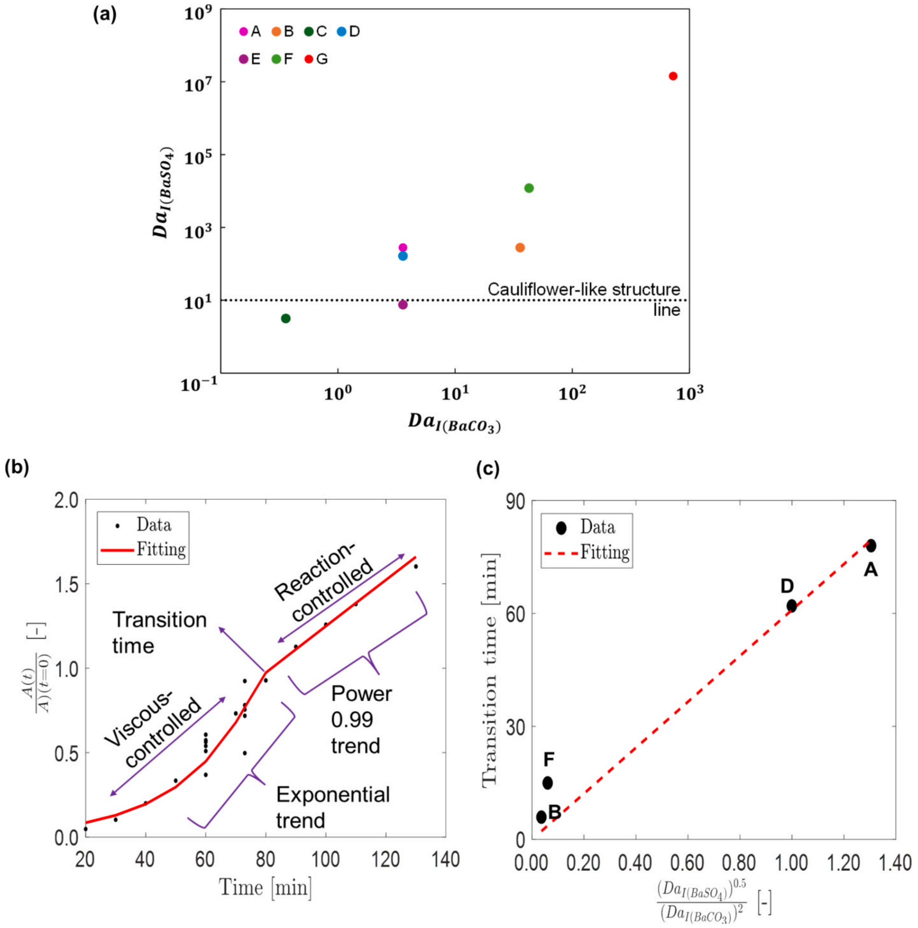

Fig. 11. Trend analysis on bubble area growth for Experiments A-F (a) Classification for each experiment based on $Da_{I(BaCO_2)}$ and $Da_{I(BaSO_4)}$ confirmed by the appearance of trapped gas bubbles; (b) An exemplary trend analysis using Experiment A data; (c) A linear correlation between transition time marking the time where the exponential growth of the bubble is constrained by the precipitated phase and $Da_{I(BaCO_2)}$, and $Da_{I(BaSO_4)}$.

4.2. Rationalizing the formation of cauliflower-like structures formation

In Experiments A – G, two competing processes underline the emergence of the cauliflower-like structures: (i) dissolution of witherite, which releases Ba^{2+} and $CO_{2(aq)}$, and (ii) precipitation of barite on the bubble surface, which consumes Ba^{2+} and promotes bubble entrapment.

Fig. 11 delineates the relationship between the two Damköhler numbers and the emergence of the “cauliflower-like structures”. The conditions favoring the emergence of “cauliflower-like structures” were identified as $\frac{Da_{IBaSO_4}}{Da_{IBaCO_3}} > 10$.

We also investigated the dynamic coupling between bubble growth and barite precipitation, which underpins bubble entrapment within the structure. These interactions exert a critical influence on both bubble size and growth kinetics. Fig. 11 presents a representative analysis from Experiment A, highlighting the trends observed in Fig. 3 and illustrating the correlation between transition time where the growth of bubble is constrained by the precipitated barite and the two Damköhler numbers. Once the system exhibits a tendency toward the formation of cauliflower-like structures, two distinct regimes of bubble area growth become apparent: an early exponential growth phase, followed by a late, power-law growth phase (Fig. 11b). Note that, before the exponential growth phase, we suspect that the system exhibits an initiation phase (Fig. 11a) which includes sufficient witherite dissolution for reaching supersaturation of gaseous CO_2 and bubble nucleation (Yamada et al., 2008). The nucleation occurs fast, forming an initial bubble that fulfills the Young-Laplace condition (Yamada et al., 2008). The early exponential growth aligns with the Rayleigh–Plesset model, where bubble radius grows as $R(t)\ e^t$ when expansion occurs against viscous forces (Favelukis and Albalak, 1996). At later times, bubble growth transitions to a power-law regime. Depending on the dominant mechanism, this follows either $R(t)\ t^{1/2}$ due to surface reactions (Favelukis and Yablonsky, 2004), or $R(t)\ t^{1/3}$ when gas generation drives bubble growth (Fu and Pan, 2009). Since we use bubble area $A(t)$ in our analysis, we can expect an exponent for time ranging between 0.67 and 1.0. We observed the variation of the time exponent value within this range in Experiment A – G (see Fig. 11b for Experiment A and Supplementary Information 2 for the other fitting results). This behavior is interpreted as indicative of a reaction-controlled growth regime.

Transition times between these two regimes (Fig. 11c) show a clear trend with:

$$t_{transition} \propto \frac{\left(Da_{I(BaSO_4)}\right)^{0.5}}{Da_{I(BaCO_2)}^{2.0}} \tag{10}$$

The transition time suggests a competition between witherite dissolution accelerating bubble growth and barite precipitation restricting its expansion. In a porous medium, this transition time indicates how the pore space changes with time, characterized by an initial rapid reduction followed by a markedly slower decrease.

4.3. Implications of the “cauliflower like structures” for energy subsurface applications

Recently, (Wegner et al., 2025) investigated the same geochemical replacement reactions in a larger configuration using core-scale column experiments. These experiments revealed a behavior similar to Experiment G, where single-phase flow transitions to a two-phase regime due to gas exsolution. A key observation was localized porosity clogging, which isolated primary witherite from further reaction despite continuous acid injection. The “cauliflower-like structures” can have significant implications for subsurface energy applications because they alter pore structure, diffusivity, and permeability, thereby influencing the long-term stability and efficiency of these systems. In hydrogen storage, iron bearing mineral precipitation, can induce pore clogging, trapping hydrogen gas, reducing storage capacity and complicating retrieval. In CO_2 sequestration, the “cauliflower effect” may cause heterogeneous CO_2 trapping, enhancing capillary trapping and mineralization, but excessive mineralization could reduce injectivity, hindering large-scale storage. In nuclear waste disposal, secondary mineral precipitation and trapped gas bubbles reduce permeability, slowing fluid flow and corrosion, similar to the shielding effect observed in Experiment G. This can improve radionuclide retention, but gas expansion may induce fractures, facilitating contaminant migration. The “cauliflower-like structures” plays central role in coupled mineral dissolution, precipitation, and gas exsolution, thereby reshaping pore structures and significantly impacting permeability and flow behavior. Our observations prompt the development of constitutive equations to describe solute transport in such chemically evolving rocks due to the “cauliflower-like structures” and will be addressed in future work. We plan to develop a numerical framework that integrates the Lattice Boltzmann method with geochemical modeling to accurately capture the coupled processes of dissolution, precipitation, and bubble growth, and to assess their consequences on permeability and diffusivity.

5. Conclusion

In this study, we developed a microfluidic platform that enables real-time visualization of coupled barite precipitation and CO_2 exsolution during witherite dissolution in acidic, sulfate-rich solutions – our defined model system. Using optical microscopy, 3D Raman imaging, and reactive transport modeling, we systematically explore the effects of pH, sulfate concentrations, flow rates, and solid-to-liquid ratios on coupled mineral dissolution with gas exsolution, identifying conditions that lead to gas entrapment or multiphase flow. Our observations reveal complex dynamics, including the emergence of CO_2 gas bubbles which get coated with a barite layer forming “cauliflower-like structures”. At low pH (≤ 1), rapid gas exsolution and barite precipitation result in extensive witherite replacement, whereas at higher pH (≥ 2), witherite dissolution occurs without significant gas formation, leading to passivation by a barite armoring layer. The interplay between the local saturation index, flow rate, and volumetric solid fraction further modulates mineral transformation. Higher sulfate concentrations and faster flow rates enhance the formation of “cauliflower-like structures”, whereas lower saturation indices inhibit gas bubble formation by preventing the CO_2 supersaturation threshold from being reached. Geochemical modeling confirms that pH and sulfate concentration govern CO_2 production and dissolution-precipitation front evolution. The “cauliflower-like structures” are observed when the ratio of Damköhler number for barite precipitation ($Da_{I(BaSO_4)}$ to the Damköhler number for witherite dissolution ($Da_{I(BaCO_2)}$) is greater than 10. These findings offer new insights into microphysical conditions controlling gas phase evolution during mineral replacement, with implications for reactive transport processes in natural and engineered systems, particularly regarding carbonate dissolution, mineral scaling, and subsurface gas migration.

Author contributions

Jenna Poonoosamy designed the experiments. Alexander Kaspor and Jenna Poonoosamy conducted the experiment. Lara Wegner conducted the Raman analysis. Jenna Poonoosamy, Alexander Kaspor, Lara Wegner did the image segmentation. Jenna Poonoosamy processed the experimental results. Dan Miron and Jenna Poonoosamy conducted the geochemical modelling. Ryan Santoso rationalized the cauliflower effect. Jenna Poonoosamy wrote the first draft of the manuscript. Jenna Poonoosamy, Ryan Santoso, Romain V.H. Dagnelie and G. Dan Miron discussed and interpreted the results, re-edited and revised the manuscript. Jenna Poonoosamy acquired the funding to conduct this investigation.

Data availability

The complete datasets generated during the current study are available from the corresponding author upon reasonable request. The datasets for graphs in Figs. 4, 5, 9, 11 can be found on the public repository EUDAT at https://doi.org/10.23728/b2share.10dkf-6vp54. While the raw data is provided in the movies as supplementary material, the segmented images can be provided upon request.

CRediT authorship contribution statement

Jenna Poonoosamy: Writing – review & editing, Writing – original draft, Visualization, Validation, Supervision, Resources, Project administration, Methodology, Investigation, Funding acquisition, Formal analysis, Data curation, Conceptualization. **Ryan Santoso:** Writing – review & editing, Formal analysis. **Alexander Kaspor:** Investigation. **Lara Wegner:** Formal analysis. **Romain V.H Dagnelie:** Formal analysis. **G.Dan Miron:** Writing – review & editing, Software.

Declaration of competing interest

The authors declare that they have no known competing financial interests or personal relationships that could have appeared to influence the work reported in this paper.

Acknowledgements

The main research leading to these results has received funding from the European Research Council through the project GENIES (ERC, grant agreement 101040341). The first author would also like to thank Master Student Andreas Seifert for preparing the movies submitted with this work, Bachelor Student Joe Jennings and Dr Guido Deissmann for a final revision of the work before submission.

Appendix A. Supplementary material

Supplementary Materials: Supplementary Information S1–2 describe in detail the mathematical equations used to calculate the relevant numbers tabulated in Table 1–2 and Figure 11. Movies 1–6 show the coupled mineral and dissolution process for the different experiments executed. Supplementary material to this article can be found online at https://doi.org/10.1016/j.gca.2025.10.025.

References

Albéric, M., Bertinetti, L., Zou, Z., Fratzl, P., Habraken, W., Politi, Y., 2018. The Crystallization of Amorphous Calcium Carbonate is Kinetically Governed by Ion Impurities and Water. Adv. Sci. 5, 1701000.

Antwi, K., Amber, I., Oluyemi, G., 2025. A coupled numerical model to assess the caprock geochemical integrity and porosity change of an underground hydrogen gas storage system. Int. J. Hydrog. Energy 109, 624–635.

Becking, L.G.M.B., Kaplan, I.R., Moore, D., 1960. Limits of the Natural Environment in terms of pH and Oxidation-Reduction Potentials. J. Geol. 68, 243–284.

Beckingham, L.E., 2017. Evaluation of Macroscopic Porosity-Permeability Relationships in Heterogeneous Mineral Dissolution and Precipitation Scenarios. Water Resour. Res. 53, 10217–10230.

Boampong, L.O., Hyman, J.D., Carey, W.J., Viswanathan, H.S., Navarre-Sitchler, A., 2024. Characterizing the combined impact of nucleation-driven precipitation and secondary passivation on carbon mineralization. Chem. Geol. 663, 122256.

Bosbach, D., 2002. Linking molecular scale barite precipitation mechanisms with macroscopic reaction rates. In: Hellmann, R.W., Scott, A. (Eds.), Water-Rock Interactions, Ore Deposits, and Environmental Geochemistry: A Tribute to David A. Geochemical Society special publication, St Louis, Crerar, pp. 97–110.

Chou, L., Garrels, R.M., Wollast, R., 1989. Comparative study of the kinetics and mechanisms of dissolution of carbonate minerals. Chem. Geol. 78, 269–282.

Deng, H., Poonoosamy, J., Molins, S., 2022. A reactive transport modeling perspective on the dynamics of interface-coupled dissolution-precipitation. Appl. Geochemistry 137, 105207.

Desarnaud, J., Bonn, D., Shahidzadeh, N., 2016. The pressure induced by salt crystallization in confinement. Sci. Rep. 6, 30856.

Everall, N.J., 2008. In confocal Raman microscopy: performance, pitfalls, and best practice, 50 years of SAS: looking to the future with vibrational spectroscopy. Louisiana, New Orleans.

Favelukis, M., Albalak, R.J., 1996. Bubble growth in viscous newtonian and non-newtonian liquids. Chem. Eng. J. 63, 149–155.

Favelukis, M., Yablonsky, G.S., 2004. Catalytic Bubble Model: Bubble Growth with an Interfacial Chemical Reaction. Ind. Eng. Chem. Res. 43, 4476–4482.

Forjanes, P., Astilleros, J.M., Fernández-Díaz, L., 2020. The Formation of Barite and Celestite through the Replacement of Gypsum. Minerals 10, 189.

Fu, B.R., Pan, C., 2009. Bubble growth with chemical reactions in microchannels. Int. J. Heat Mass Transf. 52, 767–776.

Gershenzon, N.I., Ritzi, R.W., Dominic, D.F., Mehnert, E., Okwen, R.T., 2017. Capillary trapping of CO2 in heterogeneous reservoirs during the injection period. Int. J. Greenh. Gas Control 59, 13–23.

Gholami, R., Raza, A., 2022. CO2 sequestration in sandstone reservoirs: how does reactive flow alter trapping mechanisms? Fuel 324, 124781.

Guo, X., Gin, S., Frankel, G.S., 2020. Review of corrosion interactions between different materials relevant to disposal of high-level nuclear waste. npj Mater. Degrad. 4, 34.

Guren, M.G., Putnis, C.V., Montes-Hernandez, G., King, H.E., Renard, F., 2020. Direct imaging of coupled dissolution-precipitation and growth processes on calcite exposed to chromium-rich fluids. Chem. Geol. 552, 119770.

Hannington, M., Herzig, P., Stoffers, P., Scholten, J., Botz, R., Garbe-Schönberg, D., Jonasson, I.R., Roest, W., 2001. First observations of high-temperature submarine hydrothermal vents and massive anhydrite deposits off the north coast of Iceland. Mar. Geol. 177, 199–220.

Hellmann, R., Wirth, R., Daval, D., Barnes, J.-P., Penisson, J.-M., Tisserand, D., Epicier, T., Florin, B., Hervig, R.L., 2012. Unifying natural and laboratory chemical weathering with interfacial dissolution–reprecipitation: a study based on the nanometer-scale chemistry of fluid–silicate interfaces. Chem. Geol. 294–295, 203–216.

Hulin, C., Mercury, L., 2019a. Capillarity-driven supersolubility in dual-porosity systems. Geochim. Cosmochim. Acta 252, 144–158.

Hulin, C., Mercury, L., 2019b. Regeneration of capillary water in unsaturated zones. Geochim. Cosmochim. Acta 265, 279–291.

Hummel, W., Berner, U., Curti, E., Pearson, F.J., Thoenen, T., 2002. Nagra/PSI Chemical Thermodynamic Data Base 01/01. Radiochim. Acta 90, 805–813.

Jamieson, J.W., Hannington, M.D., Tivey, M.K., Hansteen, T., Williamson, N.M.B., Stewart, M., Fietzke, J., Butterfield, D., Frische, M., Allen, L., Cousens, B., Langer, J., 2016. Precipitation and growth of barite within hydrothermal vent deposits from the Endeavour Segment, Juan de Fuca Ridge. Geochim. Cosmochim. Acta 173, 64–85.

Jiménez-Martínez, J., Hyman, J.D., Chen, Y., Carey, J.W., Porter, M.L., Kang, Q., Guthrie Jr, G., Viswanathan, H.S., 2020. Homogenization of Dissolution and Enhanced Precipitation Induced by Bubbles in Multiphase Flow Systems. Geophys. Res. Lett. 47, e2020GL087163.

Katz, G.E., Berkowitz, B., Guadagnini, A., Saaltink, M.W., 2011. Experimental and modeling investigation of multicomponent reactive transport in porous media. J. Contam. Hydrol. 120–121, 27–44.

Kilias, S.P., Nomikou, P., Papanikolaou, D., Polymenakou, P.N., Godelitsas, A., Argyraki, A., Carey, S., Gamaletsos, P., Mertzimekis, T.J., Stathopoulou, E., Goettlicher, J., Steininger, R., Betzelou, K., Livanos, I., Christakis, C., Bell, K.C., Scoullos, M., 2013. New insights into hydrothermal vent processes in the unique shallow-submarine arc-volcano, Kolumbo (Santorini). Greece. Sci. Rep. 3, 2421.

Konrad-Schmolke, M., Halama, R., Wirth, R., Thomen, A., Klitscher, N., Morales, L., Schreiber, A., Wilke, F.D.H., 2018. Mineral dissolution and reprecipitation mediated by an amorphous phase. Nat. Commun. 9, 1637.

Kulik, D.A., Wagner, T., Dmytrieva, S.V., Kosakowski, G., Hingerl, F.F., Chudnenko, K.V., Berner, U.R., 2013. GEM-Selektor geochemical modeling package: revised algorithm and GEMS3K numerical kernel for coupled simulation codes. Comput. Geosci. 17, 1–24.

Lefeuvre, N., Truche, L., Donzé, F.V., Gal, F., Tremosa, J., Fakoury, R.A., Calassou, S., Gaucher, E.C., 2022. Natural hydrogen migration along thrust faults in foothill basins: the North Pyrenean Frontal Thrust case study. Appl. Geochemistry 145, 105396.

Leroy, P., Jougnot, D., Revil, A., Lassin, A., Azaroual, M., 2012. A double layer model of the gas bubble/water interface. J. Colloid Interface Sci. 388, 243–256.

Li, C., Long, Z., Guo, D., Xie, W., Liu, L., Ma, Y., Shao, B., 2023. Catalytic mechanism of the Schikorr reaction promoted by the copper oxide nanosheet during a low-temperature hydrothermal process. Mater. Chem. Phys. 302, 127732.

Liu, J., Feng, Z., Ouyang, W., Shui, L., Liu, Z., 2022. Spontaneous Movement of a Droplet on a Conical Substrate: Theoretical Analysis of the Driving Force. ACS Omega 7, 20975–20982.

Lönartz, M.I., Yang, Y., Deissmann, G., Bosbach, D., Poonoosamy, J., 2023. Capturing the Dynamic Processes of Porosity Clogging. Water Resour. Res. 59, e2023WR034722.

Lv, C., Chen, C., Chuang, Y.-C., Tseng, F.-G., Yin, Y., Grey, F., Zheng, Q., 2014. Substrate Curvature Gradient Drives Rapid Droplet Motion. Phys. Rev. Lett. 113, 026101.

McCarthy, J., Vella, D., Castrejón-Pita, A.A., 2019. Dynamics of droplets on cones: self-propulsion due to curvature gradients. Soft Matter 15, 9997–10004.

Muniruzzaman, M., Haberer, C.M., Grathwohl, P., Rolle, M., 2014. Multicomponent ionic dispersion during transport of electrolytes in heterogeneous porous media: Experiments and model-based interpretation. Geochim. Cosmochim. Acta 141, 656–669.

Nordstrom, D.K., Alpers, C.N., Ptacek, C.J., Blowes, D.W., 2000. Negative pH and Extremely Acidic Mine Waters from Iron Mountain. California. Environ. Sci. Technol. 34, 254–258.

Osselin, F., Pichavant, M., Champallier, R., Ulrich, M., Raimbourg, H., 2022. Reactive transport experiments of coupled carbonation and serpentinization in a natural serpentinite. Implication for hydrogen production and carbon geological storage. Geochim. Cosmochim. Acta 318, 165–189.

Peng, D.-Y., Robinson, D.B., 1976. A New Two-constant Equation of State. Ind. Eng. Chem. Fundam. 15, 59–64.

Pina, C.M., Becker, U., Risthaus, P., Bosbach, D., Putnis, A., 1998. Molecular-scale mechanisms of crystal growth in barite. Nature 395, 483–486.

Poonoosamy, J., Curti, E., Kosakowski, G., Grolimund, D., Van Loon, L.R., Mäder, U., 2016. Barite precipitation following celestite dissolution in a porous medium: a SEM/BSE and μ-XRD/XRF study. Geochim. Cosmochim. Acta 182, 131–144.

Poonoosamy, J., Haber-Pohlmeier, S., Deng, H., Deissmann, G., Klinkenberg, M., Gizatullin, B., Stapf, S., Brandt, F., Bosbach, D., Pohlmeier, A., 2020a. Combination of MRI and SEM to assess changes in the chemical properties and permeability of porous media due to barite precipitation. Minerals 10, 226.

Poonoosamy, J., Kaspor, A., Schreinemachers, C., Bosbach, D., Cheong, O., Kowalski, P. M., Obaied, A., 2024. A radiochemical lab-on-a-chip paired with computer vision to unlock the crystallization kinetics of (Ba,Ra)SO4. Sci. Rep. 14, 9502.

Poonoosamy, J., Klinkenberg, M., Deissmann, G., Brandt, F., Bosbach, D., Mäder, U., Kosakowski, G., 2020b. Effects of solution supersaturation on barite precipitation in porous media and consequences on permeability: Experiments and modelling. Geochim. Cosmochim. Acta 270, 43–60.

Poonoosamy, J., Kosakowski, G., Van Loon, L.R., Mäder, U., 2015. Dissolution–precipitation processes in tank experiments for testing numerical models for reactive transport calculations: Experiments and modelling. J. Contam. Hydrol. 177–178, 1–17.

Poonoosamy, J., Lu, R., Lönartz, M.I., Deissmann, G., Bosbach, D., Yang, Y., 2022. A lab on a chip experiment for upscaling diffusivity of evolving porous media. Energies 15, 2160.

Poonoosamy, J., Mahrous, M., Curti, E., Bosbach, D., Deissmann, G., Churakov, S.V., Geisler, T., Prasianakis, N., 2021. A lab-on-a-chip approach integrating in-situ characterization and reactive transport modelling diagnostics to unravel (Ba,Sr)SO4 oscillatory zoning. Sci. Rep. 11, 23678.

Poonoosamy, J., Obaied, A., Deissmann, G., Prasianakis, N.I., Kindelmann, M., Wollenhaupt, B., Bosbach, D., Curti, E., 2023. Microfluidic investigation of pore-size dependency of barite nucleation. Commun. Chem 6, 250.

Putnis, A., Fernandez-Diaz, L., Prieto, M., 1992. Experimentally produced oscillatory zoning in the (Ba, Sr)SO4 solid solution. Nature 358, 743–745.

Putnis, C.V., Putnis, A., 2022. A mechanism of ion exchange by interface-coupled dissolution-precipitation in the presence of an aqueous fluid. J. Cryst. Growth 600, 126840.

Reese, H., Ohl, C.-D., Rosselló, J., 2024. Cavitation and jetting from shock wave refocusing near convex liquid surfaces. Int. J. Multiph. Flow 175, 104822.

Renard, F., Røyne, A., Putnis, C.V., 2019. Timescales of interface-coupled dissolution-precipitation reactions on carbonates. Geosci. Front. 10, 17–27.

Ruiz-Agudo, E., Putnis, C.V., Putnis, A., 2014. Coupled dissolution and precipitation at mineral–fluid interfaces. Chem. Geol. 383, 132–146.

Salehikhoo, F., Li, L., Brantley, S.L., 2013. Magnesite dissolution rates at different spatial scales: the role of mineral spatial distribution and flow velocity. Geochim. Cosmochim. Acta 108, 91–106.

Sanchez-Vila, X., Donado, L.D., Guadagnini, A., Carrera, J., 2010. A solution for multicomponent reactive transport under equilibrium and kinetic reactions. Water Resour. Res. 46.

Santoso, R., Guignon, L., Deissmann, G., Poonoosamy, J., 2025. Investigating the metastability of amorphous calcium carbonate by droplet microfluidics experiments using machine learning. Sci. Rep. 15, 20178.

Savelli, C., Marani, M., Gamberi, F., 1999. Geochemistry of metalliferous, hydrothermal deposits in the Aeolian arc (Tyrrhenian Sea). J. Volcanol. Geoth. Res. 88, 305–323.

Schott, J., Pokrovsky, O.S., Oelkers, E.H., 2009. The link between Mineral Dissolution/ Precipitation Kinetics and solution Chemistry. Rev. Mineral. Geochem. 70, 207–258.

Seigneur, N., Mayer, K.U., Steefel, C.I., 2019. Reactive Transport in Evolving Porous Media. Rev. Mineral. Geochem. 85, 197–238.

Soulaine, C., Roman, S., Kovscek, A., Tchelepi, H.A., 2018. Pore-scale modelling of multiphase reactive flow: application to mineral dissolution with production of $ \text{CO}_{2}$. J. Fluid Mech. 855, 616–645.

Steefel, C.I., 2019. Reactive Transport at the Crossroads. Rev. Mineral. Geochem. 85, 1–26.

Steefel, C.I., Maher, K., 2009. Fluid-Rock Interaction: a Reactive Transport Approach. Rev. Mineral. Geochem. 70, 485–532.

Steefel, C.I., Yang, L., 2021. Secondary magnesite formation from forsterite under CO2 sequestration conditions via coupled heterogeneous nucleation and crystal growth. Geochim. Cosmochim. Acta 311, 29–42.

Steinwinder, J., Beckingham, L.E., 2019. Role of Pore and Pore-Throat Distributions in Controlling Permeability in Heterogeneous Mineral Dissolution and Precipitation Scenarios. Water Resour. Res. 55, 5502–5517.

Stoffers, P., Worthington, T.J., Schwarz-Schampera, U., Hannington, M.D., Massoth, G.J., Hekinian, R., Schmidt, M., Lundsten, L.J., Evans, L.J., Vaiomo'unga, R., Kerby, T., 2006. Submarine volcanoes and high-temperature hydrothermal venting on the Tonga arc, southwest Pacific. Geology 34, 453–456.

Stryjek, R., Vera, J.H., 1986. PRSV2: a cubic equation of state for accurate vapor—liquid equilibria calculations. Can. J. Chem. Eng. 64, 820–826.

Tartakovsky, A.M., Redden, G., Lichtner, P.C., Scheibe, T.D., Meakin, P., 2008. Mixing-induced precipitation: Experimental study and multiscale numerical analysis. Water Resour. Res. 44.

Thoenen, T., Hummel, W., Berner, U., 2013. The PSI/Nagra Chemical Thermodynamic Database 12/07: present status and future developments. Mineral, Mag, p. 77.

Weber, J., Starchenko, V., Yuan, K., Anovitz, L.M., Ievlev, A.V., Unocic, R.R., Borisevich, A.Y., Boebinger, M.G., Stack, A.G., 2023. Armoring of MgO by a Passivation Layer Impedes Direct Air Capture of CO2. Environ. Sci. Technol. 57, 14929–14937.

Wegner, L., Pohlmeier, A., Wang, Y., Klinkenberg, M., Bosbach, D., Poonoosamy, J., 2025. In Situ Study of coupled Mineral Dissolution and Precipitation Processes with Gas Production in Porous Media using magnetic Resonance Imaging. Water Resour. Philos. Phenomenol. Res. 61.

Xing, Y., Brugger, J., Etschmann, B., Tomkins, A.G., Frierdich, A.J., Fang, X., 2021. Trace element catalyses mineral replacement reactions and facilitates ore formation. Nat. Commun. 12, 1388.

Xu, J., Balhoff, M.T., 2022. Novel regimes of calcium carbonate dissolution in micron-scale confined spaces. Adv. Water Resour. 164, 104200.

Xu, R., Li, R., Ma, J., He, D., Jiang, P., 2017. Effect of Mineral Dissolution/Precipitation and CO2 Exsolution on CO2 transport in Geological Carbon Storage. Acc. Chem. Res. 50, 2056–2066.

Xu, T., Senger, R., Finsterle, S., 2008. Corrosion-induced gas generation in a nuclear waste repository: Reactive geochemistry and multiphase flow effects. Appl. Geochemistry 23, 3423–3433.

Yamada, K., Emori, H., Nakazawa, K., 2008. Time-evolution of bubble formation in a viscous liquid. Earth Planets Space 60, 661–679.

Yang, Q., Sun, P.Z., Fumagalli, L., Stebunov, Y.V., Haigh, S.J., Zhou, Z.W., Grigorieva, I. V., Wang, F.C., Geim, A.K., 2020. Capillary condensation under atomic-scale confinement. Nature 588, 250–253.

Yang, Y., Churakov, S.V., Patel, R.A., Prasianakis, N., Deissmann, G., Bosbach, D., Poonoosamy, J., 2024. Pore-Scale Modeling of Water and Ion Diffusion in Partially Saturated Clays. Water Resour. Res. 60, e2023WR035595.

Zhang, Y., Cai, Y., Qu, Y., Wang, Q., Gu, L., Li, G., 2020. Two-stage fluid pathways generated by volume expansion reactions: insights from the replacement of pyrite by chalcopyrite. Sci. Rep. 10, 19993.